

***Fermi* Large Area Telescope Observations of the Supernova Remnant G8.7–0.1**

M. Ajello², A. Allafort², L. Baldini³, J. Ballet⁴, G. Barbiellini^{5,6}, D. Bastieri^{7,8}, K. Bechtol²,
R. Bellazzini³, B. Berenji², R. D. Blandford², E. D. Bloom², E. Bonamente^{9,10}, A. W. Borgland²,
J. Bregeon³, M. Brigida^{11,12}, P. Bruel¹³, R. Buehler², S. Buson^{7,8}, G. A. Caliandro¹⁴,
R. A. Cameron², P. A. Caraveo¹⁵, J. M. Casandjian⁴, C. Cecchi^{9,10}, E. Charles², A. Chekhtman¹⁶,
S. Ciprini^{17,10}, R. Claus², J. Cohen-Tanugi¹⁸, S. Cutini¹⁹, A. de Angelis²⁰, F. de Palma^{11,12},
C. D. Dermer²¹, E. do Couto e Silva², P. S. Drell², A. Drlica-Wagner², R. Dubois², C. Favuzzi^{11,12},
S. J. Fegan¹³, E. C. Ferrara²², W. B. Focke², M. Frailis^{20,23}, Y. Fukazawa²⁴, Y. Fukui²⁵,
P. Fusco^{11,12}, F. Gargano¹², D. Gasparrini¹⁹, S. Germani^{9,10}, N. Giglietto^{11,12}, P. Giommi¹⁹,
F. Giordano^{11,12}, M. Giroletti²⁶, T. Glanzman², G. Godfrey², J. E. Grove²¹, S. Guiriec²⁷,
D. Hadasch¹⁴, Y. Hanabata^{24,1}, A. K. Harding²², K. Hayashi²⁴, E. Hays²², R. Itoh²⁴,
G. Jóhannesson²⁸, A. S. Johnson², T. Kamae², H. Katagiri^{29,1}, J. Kataoka³⁰, J. Knödlseider^{31,32},
H. Kubo³³, M. Kuss³, J. Lande², L. Latronico³, S.-H. Lee³⁴, A. M. Lionetto^{35,36}, F. Longo^{5,6},
F. Loparco^{11,12}, M. N. Lovellette²¹, P. Lubrano^{9,10}, M. N. Mazziotta¹², J. Mehault¹⁸,
P. F. Michelson², T. Mizuno²⁴, A. A. Moiseev^{37,38}, C. Monte^{11,12}, M. E. Monzani², A. Morselli³⁵,
I. V. Moskalenko², S. Murgia², T. Nakamori³⁰, M. Naumann-Godo⁴, S. Nishino²⁴, P. L. Nolan²,
J. P. Norris³⁹, E. Nuss¹⁸, M. Ohno⁴⁰, T. Ohsugi⁴¹, A. Okumura^{2,40}, N. Omodei², E. Orlando^{2,42},
J. F. Ormes⁴³, D. Paneque^{44,2}, D. Parent⁴⁵, V. Pelassa²⁷, M. Pesce-Rollins³, M. Pierbattista⁴,
F. Piron¹⁸, T. A. Porter^{2,2}, S. Rainò^{11,12}, R. Rando^{7,8}, A. Reimer^{46,2}, O. Reimer^{46,2}, T. Reposeur⁴⁷,
M. Roth⁴⁸, H. F.-W. Sadrozinski⁴⁹, C. Sgrò³, E. J. Siskind⁵⁰, P. D. Smith⁵¹, G. Spandre³,
P. Spinelli^{11,12}, D. J. Suson⁵², H. Tajima^{2,53}, H. Takahashi⁴¹, T. Tanaka², J. G. Thayer²,
J. B. Thayer², L. Tibaldo^{7,8,4,54}, O. Tibolla⁵⁵, D. F. Torres^{14,56}, G. Tosti^{9,10}, A. Tramacere^{2,57,58},
E. Troja^{22,59}, Y. Uchiyama², T. Uehara²⁴, T. L. Usher², J. Vandenbroucke², A. Van Etten²,
V. Vasileiou¹⁸, G. Vianello^{2,57}, N. Vilchez^{31,32}, V. Vitale^{35,36}, A. P. Waite², P. Wang²,
B. L. Winer⁵¹, K. S. Wood²¹, H. Yamamoto²⁵, R. Yamazaki⁶⁰, Z. Yang^{61,62}, H. Yasuda²⁴,

M. Ziegler⁴⁹, S. Zimmer^{61,62}

¹Corresponding authors: Y. Hanabata, hanabata@hep01.hepl.hiroshima-u.ac.jp; H. Katagiri, katagiri@mx.ibaraki.ac.jp.

²W. W. Hansen Experimental Physics Laboratory, Kavli Institute for Particle Astrophysics and Cosmology, Department of Physics and SLAC National Accelerator Laboratory, Stanford University, Stanford, CA 94305, USA

³Istituto Nazionale di Fisica Nucleare, Sezione di Pisa, I-56127 Pisa, Italy

⁴Laboratoire AIM, CEA-IRFU/CNRS/Université Paris Diderot, Service d’Astrophysique, CEA Saclay, 91191 Gif sur Yvette, France

⁵Istituto Nazionale di Fisica Nucleare, Sezione di Trieste, I-34127 Trieste, Italy

⁶Dipartimento di Fisica, Università di Trieste, I-34127 Trieste, Italy

⁷Istituto Nazionale di Fisica Nucleare, Sezione di Padova, I-35131 Padova, Italy

⁸Dipartimento di Fisica “G. Galilei”, Università di Padova, I-35131 Padova, Italy

⁹Istituto Nazionale di Fisica Nucleare, Sezione di Perugia, I-06123 Perugia, Italy

¹⁰Dipartimento di Fisica, Università degli Studi di Perugia, I-06123 Perugia, Italy

¹¹Dipartimento di Fisica “M. Merlin” dell’Università e del Politecnico di Bari, I-70126 Bari, Italy

¹²Istituto Nazionale di Fisica Nucleare, Sezione di Bari, 70126 Bari, Italy

¹³Laboratoire Leprince-Ringuet, École polytechnique, CNRS/IN2P3, Palaiseau, France

¹⁴Institut de Ciències de l’Espai (IEEE-CSIC), Campus UAB, 08193 Barcelona, Spain

¹⁵INAF-Istituto di Astrofisica Spaziale e Fisica Cosmica, I-20133 Milano, Italy

¹⁶Artep Inc., 2922 Excelsior Springs Court, Ellicott City, MD 21042, resident at Naval Research Laboratory, Washington, DC 20375

¹⁷ASI Science Data Center, I-00044 Frascati (Roma), Italy

¹⁸Laboratoire Univers et Particules de Montpellier, Université Montpellier 2, CNRS/IN2P3, Montpellier, France

¹⁹Agenzia Spaziale Italiana (ASI) Science Data Center, I-00044 Frascati (Roma), Italy

²⁰Dipartimento di Fisica, Università di Udine and Istituto Nazionale di Fisica Nucleare, Sezione di Trieste, Gruppo Collegato di Udine, I-33100 Udine, Italy

²¹Space Science Division, Naval Research Laboratory, Washington, DC 20375-5352

²²NASA Goddard Space Flight Center, Greenbelt, MD 20771, USA

²³Osservatorio Astronomico di Trieste, Istituto Nazionale di Astrofisica, I-34143 Trieste, Italy

²⁴Department of Physical Sciences, Hiroshima University, Higashi-Hiroshima, Hiroshima 739-8526, Japan

²⁵Department of Physics and Astrophysics, Nagoya University, Chikusa-ku Nagoya 464-8602, Japan

²⁶INAF Istituto di Radioastronomia, 40129 Bologna, Italy

²⁷Center for Space Plasma and Aeronomic Research (CSPAR), University of Alabama in Huntsville, Huntsville, AL 35899

²⁸Science Institute, University of Iceland, IS-107 Reykjavik, Iceland

²⁹College of Science, Ibaraki University, 2-1-1, Bunkyo, Mito 310-8512, Japan

³⁰Research Institute for Science and Engineering, Waseda University, 3-4-1, Okubo, Shinjuku, Tokyo 169-8555, Japan

³¹CNRS, IRAP, F-31028 Toulouse cedex 4, France

³²GAHEC, Université de Toulouse, UPS-OMP, IRAP, Toulouse, France

³³Department of Physics, Graduate School of Science, Kyoto University, Kyoto, Japan

³⁴Yukawa Institute for Theoretical Physics, Kyoto University, Kitashirakawa Oiwake-cho, Sakyo-ku, Kyoto 606-8502, Japan

³⁵Istituto Nazionale di Fisica Nucleare, Sezione di Roma “Tor Vergata”, I-00133 Roma, Italy

³⁶Dipartimento di Fisica, Università di Roma “Tor Vergata”, I-00133 Roma, Italy

³⁷Center for Research and Exploration in Space Science and Technology (CRESST) and NASA Goddard Space Flight Center, Greenbelt, MD 20771

³⁸Department of Physics and Department of Astronomy, University of Maryland, College Park,

MD 20742

³⁹Department of Physics, Boise State University, Boise, ID 83725, USA

⁴⁰Institute of Space and Astronautical Science, JAXA, 3-1-1 Yoshinodai, Chuo-ku, Sagamihara, Kanagawa 252-5210, Japan

⁴¹Hiroshima Astrophysical Science Center, Hiroshima University, Higashi-Hiroshima, Hiroshima 739-8526, Japan

⁴²Max-Planck Institut für extraterrestrische Physik, 85748 Garching, Germany

⁴³Department of Physics and Astronomy, University of Denver, Denver, CO 80208, USA

⁴⁴Max-Planck-Institut für Physik, D-80805 München, Germany

⁴⁵Center for Earth Observing and Space Research, College of Science, George Mason University, Fairfax, VA 22030, resident at Naval Research Laboratory, Washington, DC 20375

⁴⁶Institut für Astro- und Teilchenphysik and Institut für Theoretische Physik, Leopold-Franzens-Universität Innsbruck, A-6020 Innsbruck, Austria

⁴⁷Université Bordeaux 1, CNRS/IN2p3, Centre d'Études Nucléaires de Bordeaux Gradignan, 33175 Gradignan, France

⁴⁸Department of Physics, University of Washington, Seattle, WA 98195-1560, USA

⁴⁹Santa Cruz Institute for Particle Physics, Department of Physics and Department of Astronomy and Astrophysics, University of California at Santa Cruz, Santa Cruz, CA 95064, USA

⁵⁰NYCB Real-Time Computing Inc., Lattingtown, NY 11560-1025, USA

⁵¹Department of Physics, Center for Cosmology and Astro-Particle Physics, The Ohio State University, Columbus, OH 43210, USA

⁵²Department of Chemistry and Physics, Purdue University Calumet, Hammond, IN 46323-2094, USA

⁵³Solar-Terrestrial Environment Laboratory, Nagoya University, Nagoya 464-8601, Japan

⁵⁴Partially supported by the International Doctorate on Astroparticle Physics (IDAPP) program

⁵⁵Institut für Theoretische Physik and Astrophysik, Universität Würzburg, D-97074 Würzburg,

Received _____; accepted _____

Accepted by ApJ. : v6.4

Germany

⁵⁶Institució Catalana de Recerca i Estudis Avançats (ICREA), Barcelona, Spain

⁵⁷Consorzio Interuniversitario per la Fisica Spaziale (CIFS), I-10133 Torino, Italy

⁵⁸INTEGRAL Science Data Centre, CH-1290 Versoix, Switzerland

⁵⁹NASA Postdoctoral Program Fellow, USA

⁶⁰Department of Physics and Mathematics, Aoyama Gakuin University, Sagamihara, Kanagawa,
252-5258, Japan

⁶¹Department of Physics, Stockholm University, AlbaNova, SE-106 91 Stockholm, Sweden

⁶²The Oskar Klein Centre for Cosmoparticle Physics, AlbaNova, SE-106 91 Stockholm, Sweden

ABSTRACT

We present a detailed analysis of the GeV gamma-ray emission toward the supernova remnant (SNR) G8.7–0.1 with the Large Area Telescope (LAT) onboard the *Fermi* Gamma-ray Space Telescope. An investigation of the relationship among G8.7–0.1 and the TeV unidentified source HESS J1804–216 provides us with an important clue on diffusion process of cosmic rays if particle acceleration operates in the SNR. The GeV gamma-ray emission is extended with most of the emission in positional coincidence with the SNR G8.7–0.1 and a lesser part located outside the western boundary of G8.7–0.1. The region of the gamma-ray emission overlaps spatially-connected molecular clouds, implying a physical connection for the gamma-ray structure. The total gamma-ray spectrum measured with LAT from 200 MeV–100 GeV can be described by a broken power-law function with a break of 2.4 ± 0.6 (stat) ± 1.2 (sys) GeV, and photon indices of 2.10 ± 0.06 (stat) ± 0.10 (sys) below the break and 2.70 ± 0.12 (stat) ± 0.14 (sys) above the break. Given the spatial association among the gamma rays, the radio emission of G8.7–0.1, and the molecular clouds, the decay of π^0 s produced by particles accelerated in the SNR and hitting the molecular clouds naturally explains the GeV gamma-ray spectrum. We also find that the GeV morphology is not well represented by the TeV emission from HESS J1804–216 and that the spectrum in the GeV band is not consistent with the extrapolation of the TeV gamma-ray spectrum. The spectral index of the TeV emission is consistent with the particle spectral index predicted by a theory that assumes energy-dependent diffusion of particles accelerated in an SNR. We discuss the possibility that the TeV spectrum originates from the interaction of particles accelerated in G8.7–0.1 with molecular clouds, and we constrain the diffusion coefficient of the particles.

Subject headings: cosmic rays — acceleration of particles — ISM: individual objects

(G8.7–0.1, HESS J1804–216) — ISM: supernova remnants — gamma rays: ISM

1. Introduction

Galactic cosmic rays are widely believed to be accelerated through the diffusive shock acceleration process at the shock of supernova remnants (SNRs) (Reynolds 2008, and references therein). It is generally expected that if a dense molecular cloud is overtaken by a supernova blast wave, the molecular cloud can be illuminated by relativistic particles accelerated at SNR shocks (e.g. Aharonian et al. 1994). If the accelerated particles are comprised mostly of protons, say > 100 times more abundant than electrons like the observed Galactic cosmic rays, decays of neutral pions produced in inelastic collisions of the accelerated protons with dense gas are expected to be a dominant radiation component in the gamma-ray spectrum of the cosmic-ray-illuminated molecular cloud. Thus, gamma-ray observations of SNRs interacting with adjacent molecular clouds are important for the study of cosmic rays.

The Large Area Telescope (LAT) onboard the *Fermi* Gamma-ray Space Telescope has recently detected GeV gamma rays from several middle-aged SNRs interacting with molecular clouds (Abdo et al. 2009, 2010b,c,h,i). The GeV emission from these SNRs is bright and spatially coincident with molecular clouds, suggesting a hadronic origin as the most plausible explanation (Abdo et al. 2009, 2010b,c,h,i). In addition, the LAT spectra of these sources exhibit spectral breaks above a few GeV and steepening above the breaks. A possible conventional mechanism for these spectral properties is the energy-dependent diffusion of accelerated particles from the SNR shell into nearby molecular clouds (e.g., Aharonian & Atoyan 1996; Gabici & Aharonian 2007; Ohira et al. 2011). On the other hand, Uchiyama et al. (2010) indicated that reaccelerated pre-existing cosmic-rays compressed at a radiative shock in a molecular cloud can explain the flat radio spectra and high gamma-ray luminosity observed in these SNRs and that the Alfvén wave evanescence due to the strong ion-neutral collisions at the shock can cause the spectral breaks. Thus, the observation of GeV gamma rays from an additional SNR in this class adds valuable information for the study of cosmic-ray acceleration in SNRs and their interactions

with surrounding matter and/or magnetic fields.

G8.7–0.1 is a middle-aged SNR located within W30 (Ojeda-May et al. 2002), a massive star forming region, and having nine discrete H II regions along the southern boundary (Blitz et al. 1982). In the radio band, the shell-like synchrotron emission has a diameter of $\sim 45'$ and a spectral index of $\alpha = 0.5$ (Kassim & Weiler 1990), suggesting that electrons are accelerated via diffusive shock acceleration. The conjunction of the molecular clouds associated with G8.7–0.1 (Blitz et al. 1982) and an OH maser on the eastern edge of the remnant (Hewitt & Yusef-Zadeh 2009) imply that the SNR is interacting with those molecular clouds. The northern part of the remnant is filled by a thermal X-ray plasma observed by *ROSAT* (Finley & Oegelman 1994). The distance to G8.7–0.1 is estimated to be ~ 4.8 –6 kpc based on kinematic distances to the H II regions associated with the SNR (Kassim & Weiler 1990; Brand & Blitz 1993) and 3.2–4.3 kpc based of the SNR evolution with the observed X-ray temperature and the angular radius (Finley & Oegelman 1994). The age of the SNR is estimated to be 1.5 – 2.8×10^4 yr based on applying a Sedov solution to the X-ray observation under the assumption of an initial kinetic energy of 10^{51} erg (Finley & Oegelman 1994), or alternatively, 1.5×10^4 yr using the relation between the age and the surface brightness (Odegard 1986). In this paper, we adopt an age of 2.5×10^4 yr.

The HESS collaboration found a TeV gamma-ray source in the vicinity of G8.7–0.1, HESS J1804–216, which has an extension of $22'$ (Aharonian et al. 2006) and has been confirmed by CANGAROO-III (Higashi et al. 2008). This source lacks an evident counterpart and is classified as unidentified. Gabici & Aharonian (2007) predicts that a number of TeV unidentified sources might be explained by molecular clouds illuminated by cosmic rays escaping from a nearby SNR. Thus, the relationship between HESS J1804–216 and G8.7–0.1 is interesting for probing the diffusion process of cosmic rays assuming that G8.7–0.1 is a probable cosmic-ray accelerator. Measurements with the Energetic Gamma-Ray Experiment Telescope (EGRET)

onboard the *Compton Gamma-ray Observatory* found no gamma-ray sources around G8.7–0.1. A gamma-ray source is listed around G8.7–0.1 in the Astro-rivelatore Gamma a Immagini LEggero (AGILE) one year catalog (Pittori et al. 2009). However, AGILE has not published a detailed analysis of this field. Three LAT sources in the vicinity of G8.7–0.1 are listed in the 1FGL catalog (Abdo et al. 2010d), which is compiled under the assumption that sources are point-like. 1FGL J1805.2–2137c was studied by Castro & Slane (2010) as the SNR with a point-like assumption.

In this paper, we report a detailed analysis of the LAT sources around G8.7–0.1 based on 23-months data. First, we give a brief description of the gamma-ray selection in Section 2. The analysis procedures and results are explained in Section 3, including measurements of the spatial extension and spectra of the LAT sources near the remnant. The discussion is given in Section 4, followed by conclusions in Section 5.

2. OBSERVATION & DATA REDUCTION

The LAT is the main instrument on *Fermi*. The energy band extends from ~ 20 MeV to > 300 GeV¹. It is an electron-positron pair production telescope consisting of layers of tungsten foils and silicon microstrip detectors to measure the arrival directions of incoming gamma rays, and a hodoscopic cesium iodide calorimeter to determine the gamma-ray energies. The instrument is surrounded by 89 plastic scintillator tiles that serve as an anticoincidence detector for rejecting charged particle events. Details of the LAT instrument and pre-launch expectations of the performance can be found in Atwood et al. (2009). Relative to earlier gamma-ray missions, the LAT has a large ~ 2.4 sr field of view, a large effective area (~ 8000 cm² for >1 GeV if on-axis), and improved angular resolution with a point spread function (PSF) described by a 68%

¹As noted below in the present analysis we use only events with energies > 200 MeV.

containment angle better than 1° at 1 GeV.

Routine science operations of the LAT began on August 4, 2008, after the conclusion of a commissioning period. We have analyzed events around G8.7–0.1 collected from August 4, 2008, to July 9, 2010, with a total exposure of $\sim 5.5 \times 10^{10} \text{ cm}^2 \text{ s}$ (at 1 GeV). During this time interval, the LAT was operating in sky survey mode nearly all of the time, obtaining complete sky coverage every 2 orbits (~ 3 hours) and relatively uniform exposure over time.

We used the standard LAT analysis software, *ScienceTools* v9r15, which is available from the *Fermi* Science Support Center (FSSC)², and applied the following event selection criteria: 1) events should have the highest probability of being gamma rays, i.e., they should be classified as so-called *Diffuse* class (Atwood et al. 2009), 2) the reconstructed zenith angles of the arrival direction of gamma rays should be less than 105° to minimize contamination by gamma rays from the limb of the Earth, 3) the center of the LAT field of view should be within 52° of zenith in order to exclude data from the short time intervals when the field of view contains a larger portion of the Earth. No gamma-ray bursts were detected by the LAT within 15° of G8.7–0.1; thus, we did not need to apply any additional time cut. The energy range analyzed here is restricted to $> 200 \text{ MeV}$ to avoid possible large systematic uncertainties at lower energies due to the strong Galactic diffuse emission (especially for G8.7–0.1, which lies in the direction of the Galactic center), smaller effective area, and broader PSF.

²Software and documentation of the *Fermi ScienceTools* are distributed by *Fermi* Science Support Center at <http://fermi.gsfc.nasa.gov/ssc>

3. ANALYSIS AND RESULTS

3.1. Morphological Analysis

Figure 1 shows a smoothed count map in the 2–10 GeV energy band in a $10^\circ \times 10^\circ$ region around G8.7–0.1. The average surface brightness of this region is about 2 times larger than neighboring regions along the Galactic plane. There are three LAT sources in the vicinity of G8.7–0.1 in the 1FGL catalog (Abdo et al. 2010d): 1FGL J1805.2–2137c and 1FGL J1806.8–2109c located to the east, and 1FGL J1803.1–2147c located to the west.

In order to evaluate the source extension and location of these three sources, we used the maximum likelihood tool, `gtlike`, which is available as part of the *Fermi ScienceTools*. The likelihood is the product of the probabilities of observing the gamma-ray counts within each spatial and energy bin for a specified emission model. The best parameter values are estimated by maximizing the likelihood of the data describing the given model (Mattox et al. 1996). The probability density function for the likelihood analysis includes 1) individual sources detected in the 1FGL catalog within 15° of G8.7–0.1, 2) the Galactic diffuse emission resulting from cosmic-ray interactions with interstellar medium and radiation based on the LAT standard diffuse background model *gll_iem_v02* available from the FSSC³, and 3) an isotropic component to represent extragalactic gamma rays and residual instrumental backgrounds using the standard isotropic spectral template *isotropic_iem_v02* also available from the FSSC. The region of interest for the binned maximum likelihood analysis was a square region of $20^\circ \times 20^\circ$ in Galactic coordinates centered on G8.7–0.1 with a pixel size of 0.1° . The instrument response functions (IRFs) used in our work were the “Pass 6 v3 Diffuse” (P6_V3_DIFFUSE) IRFs; a post-launch update to address gamma-ray detection inefficiencies that are correlated with

³The model can be downloaded from
<http://fermi.gsfc.nasa.gov/ssc/data/access/lat/BackgroundModels.html>.

background rates. Since PSR J1809–2332 (Abdo et al. 2010f) and W28 (Abdo et al. 2010h) are the brightest sources in the region of interest, they must be carefully modeled to perform the morphological studies. Their spectral shapes were modeled as a power-law with an exponential cutoff and a broken power-law, respectively. A spatial template was used for W28 to take into account its extension (Abdo et al. 2010h).

Before investigating the extension in detail, we first determined the strength of the diffuse gamma-ray emission around G8.7–0.1 by using the tools described above. The morphology analysis included only events above 2 GeV to take advantage of the narrower PSF at higher energies. We determined the flux and spectral parameters for all model components. In this process, the normalization of the Galactic diffuse emission and the flux and spectral index of a power-law model for the sources within 4° of the direction of G8.7–0.1 were set free to account for the effects of the sources nearest to G8.7–0.1 on the fit. The spectral parameters for more distant sources were fixed to the values in the 1FGL catalog. The flux and spectral parameters were then fixed, with the exception of those for the three sources overlapping G8.7–0.1. Figure 2 shows a close-up view of the counts map around G8.7–0.1 in the 2–10 GeV band with the diffuse emission subtracted. Contours representing the radio emission, CO line intensity and TeV gamma-rays are overlaid on the GeV gamma-ray map.

The coincidence of 1FGL 1805.2–2137c and 1FGL 1806.8–2109c with the eastern enhancement in the GeV counts map suggested extension of the emission. To evaluate the presence and size of an extended source, we modeled it as a uniform disk. We varied the radial size and centroid of the disk while holding the position of neighboring 1FGL 1803.1–2147c fixed at the catalog values, and evaluated the resulting maximum likelihood value (L_{ex}) with respect to the maximum likelihood for the no-source hypothesis (L_0). The largest likelihood ratio, $-2\ln(L_0/L_{\text{ex}})$ (9 degrees of freedom) of ≈ 478 was obtained for a disk radius σ of $0^\circ.37$. This is substantially better than that obtained for a model containing two point sources, $-2\ln(L_0/L_{2s})$ (12

degrees of freedom) ≈ 433 , where L_{2s} is the likelihood for two sources instead of a disk shape, whose positions were free in the optimization. Therefore, we conclude that the eastern part of the GeV emission is significantly extended. Hereafter, we refer to the emission as Source E and employ a uniform disk as the spatial model for further analysis. The best-fit centroid for the disk model in J2000 is found to be (R.A., decl.) = ($18^{\text{h}}05^{\text{m}}.6$, $-21^{\circ}38'.0$) with an error radius of $0^{\circ}028$ at the 68 % confidence level.

The extension of the third source, 1FGL 1803.1–2147c, (hereafter, Source W) was also investigated using the same procedure as above. We did not find significant extension in that case. An upper limit on the spatial extent of the gamma-ray emission was obtained by investigating the decrease of maximum likelihood with increasing radial size of the source in the input emission model. Under the assumption of a uniform disk, the upper limit on the radius was $22'$ at the 68 % confidence level. The best-fit location for Source W in J2000 was estimated to be (R.A., decl.) = ($18^{\text{h}}03^{\text{m}}.3$, $-21^{\circ}47'.8$) with an error radius of $0^{\circ}038$ at the 68 % confidence level.

To quantitatively evaluate the correlation of the GeV emission with other wavebands, we also performed the likelihood analysis using spatial templates derived in those bands in place of the best-fit models derived above. We calculated the maximum likelihood for a VLA radio image at 90 cm (Brogan 2006) with a point source added to model Source W since it does not appear to have a radio counterpart. We additionally calculated the maximum likelihood using the background-subtracted counts map of TeV gamma rays measured by HESS (Aharonian et al. 2006). To allow for background fluctuations in the VLA and HESS templates, the fits were performed by changing the extracted regions of the templates (see Table 1). A simple power-law function was assumed for the spectral models of the above spatial templates. Note that we did not use the CO images to form spatial templates since they inevitably contain large amounts of matter unrelated to the gamma-ray emission from the remnant. The resulting maximum likelihood values with respect to the null hypothesis (no emission associated with G8.7–0.1) are summarized

in Table 1. The likelihood ratio for the radio image is higher than for the model containing three point sources, while the likelihood ratio for the HESS image is significantly lower. Therefore, we conclude that the radio morphology correlates reasonably well with the GeV emission while the TeV morphology does not.

3.2. Energy Spectrum

We used the maximum likelihood fit tool, `gtlike`, for the spectral analysis of the LAT sources. In order to produce a spectral energy distribution (SED) in a model-independent manner, fits were performed in eight logarithmically spaced-energy bins covering energies from 200 MeV to 100 GeV. Within each energy bin we fixed the spectral index at 2 for the LAT sources. Note that the flux within an energy bin can vary up to $\sim 10\%$ depending on the choice of spectral index and is taken into consideration as a systematic error.

The resulting SEDs for Source E and Source W are shown in Figure 3. The overlap with the spatially-connected molecular clouds suggests that there might be a physical connection; thus, we also obtained the total SED of the two sources together, as shown in Figure 3.

We accounted for systematic errors caused by uncertainties in the extension, the Galactic diffuse model, and the LAT effective area. Systematic errors associated with the extension were estimated by varying the size of Source E by $\pm 1\sigma$. We considered the energy and positional dependence for the systematic errors of the Galactic diffuse model. The energy dependence was estimated by using the residual gamma-ray data with respect to the best-fit model in a region where no LAT source is present. We used the neighboring regions on both sides of G8.7–0.1 along the Galactic plane (see Figure 1); (i) $l = 7^\circ.1\text{--}7^\circ.7$ and $b = -1^\circ.1\text{--}0^\circ.9$, (ii) $l = 9^\circ.15\text{--}9^\circ.75$ and $b = -1^\circ.1\text{--}0^\circ.9$. The observed residual can be modeled as $\sim (100 (E/1 \text{ GeV})^{1.89 \times 10^{-2}} - 100) \%$ and $\sim (101 (E/1 \text{ GeV})^{-0.89 \times 10^{-2}} - 100) \%$ of the total Galactic diffuse flux for (i) and (ii),

respectively. The normalization of the Galactic diffuse model was adjusted according to the above equations to estimate the systematic error on the source flux. On the other hand, the positional dependence of this residual was estimated by Abdo et al. (2010i) and found to be $\sim 6\%$. We evaluated the systematic errors due to positional dependence by varying the normalization of the Galactic diffuse model by $\pm 6\%$ from the best fit value. We also evaluated systematic errors due to uncertainties in the LAT effective area, which are 10% at 100 MeV, decreasing to 5% at 500 MeV, and increasing to 20% at 10 GeV and above (Rando et al. 2009). The combined systematic errors on the flux are shown by the black bars in Figure 3.

We evaluated the possibility of a spectral break for the combined LAT source, i.e., the sum of Source E and Source W, in the LAT energy band by comparing the likelihood of a simple power-law model and a smoothly broken power-law model for both sources. The smoothly broken power-law model was described as

$$\frac{dN}{dE} = KE^{-\Gamma_1} \left(1 + \left(\frac{E}{E_{\text{break}}} \right)^{\frac{\Gamma_2 - \Gamma_1}{\beta}} \right)^{-\beta}, \quad (1)$$

where the photon indices, Γ_1 below the break and Γ_2 above the break, the break energy E_{break} , and the normalization factor K were free parameters. The parameter β was held fixed at 0.05. To treat Source E and Source W as a combined source, the spectral parameters were varied jointly with the exception of the flux normalizations, which were allowed to vary independently. The fit yields a likelihood ratio $-2 \ln(L_{\text{PL}}/L_{\text{BPL}}) \approx 32$, where L_{PL} and L_{BPL} are the likelihoods for the simple power-law model and the smoothly broken power-law model, respectively. In a worst-case scenario enforcing 1σ systematic uncertainties, the likelihood ratio decreases to ~ 23 (corresponding to 4.4σ with 2 degrees of freedom). The best-fit parameters obtained for the smoothly broken power-law model were photon indices $\Gamma_1 = 2.10 \pm 0.06$ (stat) ± 0.10 (sys), $\Gamma_2 = 2.70 \pm 0.12$ (stat) ± 0.14 (sys), and $E_{\text{break}} = 2.4 \pm 0.6$ (stat) ± 1.2 (sys) GeV.

We also investigated the spectral shape of each source separately. The best-fit spectral parameters for Source E were found to be $\Gamma_1 = 2.10 \pm 0.11$ (stat) ± 0.12 (sys), $\Gamma_2 = 2.47 \pm 0.09$

(stat) \pm 0.13 (sys), and $E_{\text{break}} = 1.8 \pm 0.7$ (stat) \pm 0.7 (sys) GeV, while those for Source W were found to be $\Gamma_1 = 2.08 \pm 0.15$ (stat) \pm 0.25 (sys), $\Gamma_2 = 5.88 \pm 1.67$ (stat) \pm 1.27 (sys), and $E_{\text{break}} = 4.5 \pm 0.3$ (stat) \pm 0.1 (sys) GeV. Thus, we cannot conclude with the present data that the spectral shapes differ significantly since the break energy of Source E and the Γ_2 of Source W have large errors. The smoothly broken power-law models above give detection significances for Source E and Source W in the 200 MeV–100 GeV of 28σ and 16σ , respectively.

We investigated the spectral connection between the GeV and TeV energy bands. Here, we used a chi-squared test for the spectral fit of the LAT data and the HESS measurements (Aharonian et al. 2006). A fit assuming a broken power-law model yields a null-hypothesis probability of less than 1.0×10^{-18} , including the worst-case 1σ systematic uncertainties. We conclude that the GeV spectrum does not connect to the HESS measurements smoothly.

3.3. Time Variability and Pulsation Search of the LAT Source

Source W could not be spatially resolved by our work, so other gamma-ray source candidates must be considered. We checked the time variability of Source W to test the hypothesis of a background active galactic nuclei. We divided the data into two-month intervals and fit for the flux of Source W. The flux showed no significant time variability, indicating a steady source of emission for this time scale and making it less likely to be a gamma-ray blazar.

We also checked for previously undetected gamma-ray pulsars in this region. The ATNF database (Manchester et al. 2005)⁴ lists two nearby radio pulsars with a spin-down power \dot{E} typical of the known gamma-ray pulsars: PSR J1803–2137 (Clifton & Lyne 1986) and PSR J1806–2125 (Hobbs et al. 2002) as shown in Figure 2. PSR J1803–2137 has $\dot{E} = 2.2 \times 10^{36}$ erg s^{−1} and a nominal distance of 3.88 kpc derived from the Dispersion Measure

⁴<http://www.atnf.csiro.au/research/pulsar/psrcat>

(DM) using NE2001 (Cordes & Lazio 2002), while PSR J1806–2125 has $\dot{E} = 4.3 \times 10^{34}$ erg s^{−1} and an estimated distance of 9.85 kpc. Considering the above values, the latter is not expected to emit a detectable gamma-ray flux. Using rotational ephemerides provided by the Parkes (Weltevrede et al. 2010), Nancay (Theureau et al. 2005), and Jodrell Bank (Hobbs et al. 2004) radio telescopes, we phase-folded the gamma-ray data, but found no evidence for gamma-ray pulsations.

The observed properties of gamma-ray pulsars (Abdo et al. 2010f) suggest that PSR J1803–2137 could have a flux of 9.1×10^{-8} ph cm^{−2} s^{−1} above 100 MeV. To check explicitly for the presence of emission from this source, we performed likelihood fits with an additional point source modeled at the position of PSR J1803–2137. The spectral model was assumed to be a power-law with an exponential cutoff and the normalization was set free while the spectral index and cutoff energy were fixed at 1.5 and 2 GeV, the average values in the Fermi 1st Pulsar catalog (Abdo et al. 2010f). The likelihood was not improved with the addition of the pulsar to the model. In the absence of a detection, we set an upper limit on the flux at the 90% confidence level of 1.0×10^{-8} ph cm^{−2} s^{−1} above 100 MeV and conclude that the pulsar does not significantly contribute to the GeV emission.

Abdo et al. (2010f) calculated a 5σ flux sensitivity for pulsations to be detected by a blind search of six months of LAT data. The general upper limit for the Galactic plane of $\simeq 2.0 \times 10^{-7}$ photons cm^{−2} s^{−1} above 100 MeV is similar to the flux of Source W. Therefore, we cannot completely exclude the possibility that Source W is a gamma-ray pulsar. The above results in combination with the observed extension of Source E imply that the bulk of the gamma ray emission near the remnant does not come from an undetected gamma-ray pulsar.

4. DISCUSSION

4.1. Origin of the GeV Emission

4.1.1. *Assumptions for Spectral Modeling*

We have analyzed the GeV gamma rays in the vicinity of G8.7–0.1 and found the emission to be significantly extended. The bulk of the emission (Source E) is positionally coincident with the synchrotron radio emission from the SNR G8.7–0.1, while a lesser part (Source W), located outside the western boundary of G8.7–0.1, has no obvious counterpart within the 95% confidence region obtained by a point source model. The GeV morphology is reasonably well represented by the radio emission of the SNR, suggesting a correlation with high-energy electrons. There are molecular clouds spatially associated with G8.7–0.1 (Blitz et al. 1982) and likely to be interacting with the SNR since an OH maser is detected on the eastern edge of G8.7–0.1 (Hewitt & Yusef-Zadeh 2009). The GeV gamma rays overlap with these spatially-connected molecular clouds. This implies a physical connection of the two LAT sources although there remains a possibility that Source W is a gamma-ray pulsar undetected at the current sensitivity. Here, we assume that the bulk of GeV gamma-rays comes from the interaction between particles accelerated by the SNR and gas in the clouds, where the particles are confined in the SNR shell. Also, we assume that the molecular clouds uniformly cover the whole surface of the SNR since the CO emission is not significantly localized in any part of the SNR. Note that since the eastern part of this region dominates the GeV emission, the contribution of the western source does not affect any conclusions drawn in this paper. We discuss the possibility that the GeV gamma-rays come from other sources in Section 4.1.3.

The TeV gamma-ray source, HESS J1804–216, overlaps the GeV gamma rays. However, the TeV morphology is not better correlated with the GeV gamma rays than the radio emission from G8.7–0.1 and the GeV spectrum does not connect smoothly to the TeV spectrum, indicating

another emission component, either additional high-energy particles accelerated by G8.7–0.1 or a high-energy source unrelated to G8.7–0.1. In section 4.1, we focus on the GeV emission and reserve discussion of the relation between the TeV and GeV emission for Section 4.2.

Below, we adopt the simplest assumption, that a population of accelerated protons and electrons is distributed in a region characterized by constant density and magnetic field strength and the injected electrons have the same momentum distribution as the protons. This assumption implies a break in the particle momentum spectrum because the spectral index of the radio data, which corresponds to lower particle momenta, is much harder than that of the gamma-rays, which correspond to higher particle momenta. We use the following functional form to model the momentum distribution of injected particles:

$$Q_{e,p}(p) = a_{e,p} \left(\frac{p}{1 \text{ GeV } c^{-1}} \right)^{-s_L} \left(1 + \left(\frac{p}{p_{\text{br}}} \right)^2 \right)^{-(s_H - s_L)/2}, \quad (2)$$

where p_{br} is the break momentum, s_L is the spectral index below the break and s_H above the break. Note that here we consider the minimum momenta of protons and electrons to be $100 \text{ MeV } c^{-1}$ since the details of the proton/electron injection process are poorly known.

Electrons suffer energy losses due to ionization (or Coulomb scattering), bremsstrahlung, synchrotron processes, and IC scattering. The modification of the electron spectral distribution due to such losses was calculated according to Atoyan et al. (1995), where electrons are assumed to be injected at $t = 0$ from an impulsive source. Since diffusive shock acceleration theory generally predicts particle acceleration in the Sedov phase with a typical duration 10^3 – 10^4 yr, the assumption of an impulsive source is a good approximation for G8.7–0.1, which has an age of 2.5×10^4 yr. Note that we ignore the radiative cooling of protons since the time scale of the energy loss due to nuclear interaction is $\approx 6 \times 10^7 (1 \text{ cm}^{-3}/\bar{n}_H) \text{ yr}$ (Aharonian & Atoyan 1996), which is much greater than the SNR age unless the environment is very dense. We adopt 4 kpc for the distance from the Earth to the SNR since the GeV emission overlaps molecular clouds corresponding to a kinematic distance of 3.5–4.5 kpc. The gamma-ray spectrum from π^0 decays

produced by the interaction of protons with ambient hydrogen is scaled by a factor of 1.84 to account for helium and heavy nuclei in the target material and the cosmic-ray composition (Mori 2009). We also consider the contribution of the emission from secondary e^+/e^- produced by charged pion production and decay in the π^0 decay model. For the calculation of spectra of the secondaries, we use the parametric formulae from Kamae et al. (2006).

4.1.2. SNR G8.7–0.1

First, we consider a π^0 -decay model to account for the broadband gamma-ray spectrum. We use an electron-to-proton ratio of $K_{ep} = 0.01$, which is the ratio found in the local cosmic-ray abundance. Here the ratio is defined at a particle momentum of 1 GeV c^{-1} . The spectral index of proton momentum in the high-energy regime is constrained to be $s_H \approx 2.7$ from the gamma-ray spectral slope. The index below the break is determined to be $s_L \approx 2.0$ by the observed radio spectrum due to synchrotron radiation by relativistic electrons (Kassim & Weiler 1990). Note that we do not account for the spectral turnover at radio frequencies which is due to absorption by localized thermal gas associated with one or more of the H II regions near the W30 complex (Kassim & Weiler 1990). The observed gamma-ray luminosity requires the gas density to be much larger than $\bar{n}_H \approx 1 \text{ cm}^{-3}$ averaged over the entire SNR shell in order not to exceed the typical kinetic energy of a supernova explosion ($\sim 10^{51} \text{ erg}$). We assume $\bar{n}_H = 100 \text{ cm}^{-3}$ which is a typical value in molecular clouds. This is consistent with CO observations because the mass of a shell of radius 26 pc⁵ and thickness 7 pc⁶ with density \bar{n}_H is $1.9 \times 10^5 M_\odot$ which

⁵This is estimated with the apparent diameter of the SNR and the distance of G8.7–0.1 to the Earth.

⁶This is constrained by the apparent distance from the edge of the radio emission to the position of Source W.

is smaller than the value of $5.9 \times 10^5 M_\odot$ estimated from the CO data taken by the NANTEN telescope (Mizuno & Fukui 2004; Takeuchi et al. 2010).

Using the parameters summarized in Table 2, we calculated radiation model curves as shown in Figure 4 (a). The resulting total proton energy, $W_p \sim 2.8 \times 10^{49} \cdot (10^2 \text{ cm}^{-3}/\bar{n}_H) \cdot (d/4 \text{ kpc})^2 \text{ erg}$, is less than 10% of the typical kinetic energy of a supernova explosion and quite reasonable. Note that W_p is not the total energy of accelerated protons but that of the in-situ protons in the molecular clouds. W_p is changed up to a factor of ~ 2 within the uncertainty of its distance (3.2–6 kpc), which does not affect our conclusion. It is difficult to derive the break point of the proton momentum spectrum from the break in the gamma-ray spectrum since it lies in the region where we expect a gamma-ray spectral curvature due to the kinematics of π^0 production and decay. The gamma-ray spectrum gives an upper bound for the momentum break at $\sim 10 \text{ GeV } c^{-1}$. The momentum break cannot be lower than $\sim 3 \text{ GeV } c^{-1}$ to avoid conflict with the radio data. Here we adopt $3 \text{ GeV } c^{-1}$. The magnetic field strength is constrained to be $B \sim 100 \mu\text{G}$, which is plausible since a magnetic field can be amplified up to several hundred μG by the compression of gas by the shock of a middle-aged SNR in molecular clouds (Chevalier 1999). The emission from secondary e^+/e^- does not significantly contribute to the emission from G8.7–0.1 in this modeling given the above \bar{n}_H .

To consider the situation when the synchrotron emission from the secondaries dominates in the radio band, we model the GeV emission with $\bar{n}_H = 1000 \text{ cm}^{-3}$. Although the mass of the molecular clouds with the assumed shape exceeds the value estimated by using the NANTEN data in this case, that \bar{n}_H is possible if the clouds responsible for the GeV emission have nonuniform structure. The modeling results are shown in Table 2 and Figure 4(b), respectively. The range of the momentum break changes slightly to 3–15 $\text{GeV } c^{-1}$ and the magnetic field is constrained to be $\sim 400 \mu\text{G}$. From the above considerations, the π^0 decay model can explain the GeV emission although the magnetic field and the momentum break depend on \bar{n}_H .

Leptonic models struggle to match the GeV gamma-ray spectrum. The electron-bremsstrahlung dominated model (Figure 4(c)) cannot explain the GeV gamma rays unless K_{ep} of the accelerated particles is much larger than ~ 0.01 , as found in the local cosmic-ray abundance. For the inverse Compton (IC) dominated model (Figure 4(d)), the total energy in electrons is calculated to be $W_e \approx 9.9 \times 10^{50} \cdot (d/4 \text{ kpc})^2 \text{ erg}$, for an energy density of $\sim 2.9 \text{ eV cm}^{-3}$ for the interstellar radiation field⁷, which is comparable to the typical kinetic energy of a supernova explosion ($\sim 10^{51} \text{ erg}$). Therefore, the IC dominated model is not plausible unless the radiation field is at least 10 times more intense than expected.

Assuming the π^0 -decay model, our observations of the LAT source in the vicinity of G8.7–0.1 when combined with the radio data constrain the proton momentum break to be in the range 3–15 GeV c^{-1} . This spectral feature might indicate the escape of the accelerated particles confined around the blast waves propagating into the dense clouds (e.g., Uchiyama et al. 2010). On the other hand, Gabici & Aharonian (2007) discussed the time evolution of non-thermal emission from molecular clouds illuminated by cosmic rays from a nearby SNR and predicted a steep gamma-ray spectrum for an old SNR due to energy-dependent diffusion of cosmic rays. The two models do not produce the emission at the same place. In the former, the gamma-ray emission comes from the cloud shock, which can be traced by non-thermal radio filaments. However, the spatial difference is too small to be resolved by the LAT. Therefore, we cannot say which model is favorable for the GeV emission.

⁷The interstellar radiation field (see Table 2) for non cosmic microwave background at the location of G8.7–0.1 is estimated from the GALPROP code (Porter et al. 2008) with approximation of two infrared and two optical blackbody components.

4.1.3. *Other Sources*

First, we consider the possibility that the GeV gamma rays come from pulsar wind nebulae (PWNe). The IC emission from relativistic electrons is the most plausible process for the gamma-ray emission from PWNe (Abdo et al. 2010a,e,g; Slane et al. 2010; Grondin et al. 2011). A PWN nearer to the Earth than the location of G8.7–0.1 is a possible candidate since the smaller distance loosens the constraint on energetics derived from an IC dominated model. There are several known or suspected PWNe in this field, one associated with PSR J1803–2137 (Kargaltsev et al. 2007) and another a PWN candidate found with Suzaku, J1804–2140 (Bamba et al. 2007), which were found only in the X-ray band. If the IC emission contributes significantly to such a bright GeV source, then the synchrotron emission in the radio band due to the corresponding electrons would be detectable unless the magnetic field is weaker than $\sim 1 \mu\text{G}$. Magnetic fields in PWNe with GeV emission are estimated to be at least $\sim 3 \mu\text{G}$ using the *Fermi* LAT observations (Abdo et al. 2010a,e,g; Slane et al. 2010; Grondin et al. 2011). Thus, we suppose that the bulk of the GeV emission does not come from a PWN.

Next, we consider the contribution of SNR G8.31–0.09, which has a small size of $5' \times 4'$ (Brogan 2006). This SNR is not located at the bright portion of the GeV emission. Therefore, we conclude that gamma-ray emission from G8.31–0.09 cannot significantly contribute to the GeV emission. From these considerations, the bulk of the GeV gamma rays is most naturally explained by the decay of π^0 s produced by the interaction of G8.7–0.1 with molecular clouds.

4.2. Origin of the TeV Emission

4.2.1. Pulsar Wind Nebula

We consider the relation between the TeV gamma-ray source, HESS J1804–216, and the GeV emission. One possibility is that the TeV emission arises via the IC scattering of the relativistic electrons in a PWN. The sizes of the PWNe found in the X-ray, which have extension of at most $\sim 2'$ (Kargaltsev et al. 2007; Bamba et al. 2007), are ~ 40 times smaller than the extension of the TeV gamma-ray source. TeV emission from the IC process can be more extended than synchrotron X-ray emission from a PWN due to differences in radiative cooling times for the electrons generating the emission in those bands (de Jager & Djannati-Ataï 2008). In the case of the PWN associated with PSR J1803–2137, the extended TeV gamma-ray emission ($\sim 30 \text{ pc}^8$) can be explained if the transporting velocity for the TeV-emitting electrons averaged over the age of the pulsar (15.6 kr; Brisken et al. (2006)) is larger than $\sim 1900 \text{ km s}^{-1}$. Diffusion parallel to a magnetic field, or convection might explain such a large propagation velocity (de Jager & Djannati-Ataï 2008). On the other hand, the Suzaku J1804–2140 PWN is not well-studied and its origin remains unclear. Therefore, we cannot rule out the possibility of a PWN origin for the TeV emission.

4.2.2. Cosmic Rays Accelerated in G8.7–0.1

Another possibility is that the TeV emission also originates in the particles accelerated in G8.7–0.1. It is predicted that TeV gamma-ray emission can arise from the interaction of cosmic rays that have escaped from an SNR with nearby molecular clouds, say within $\sim 100 \text{ pc}$ (e.g,

⁸The extension is estimated by the apparent size and the distance of 3.88 kpc from the Earth to the pulsar

Aharonian & Atoyan 1996). On the other hand, we argue in Section 4.1 that the GeV emission comes from the interaction of particles confined in the shell of G8.7–0.1 with molecular clouds. A combined scenario can explain the concave spectral shape in the GeV–TeV band, i.e., the molecular clouds distant from G8.7–0.1 along the line of sight emit the TeV gamma rays, while the molecular clouds responsible for the GeV emission are located adjacent to the SNR. The spectral index of 2.72 ± 0.06 for the TeV gamma rays (Aharonian et al. 2006) is consistent with the particle spectral index predicted by a theory assuming the energy-dependent diffusion of particles accelerated in an SNR (e.g., Aharonian & Atoyan 1996), supporting the above scenario. If this is correct, we can constrain the diffusion coefficient.

We performed the modeling for the GeV and TeV gamma-ray spectra considering the above scenario. Again, we treat G8.7–0.1 as an impulsive source injecting the accelerated particles at $t = 0$. In addition, we assume that the accelerated particles do not escape into interstellar space until the SNR enters the Sedov phase at t_{Sedov} . Under the above assumptions, the density spectrum of diffused protons is derived by Gabici et al. (2009) as:

$$f(E, R, t) = \frac{N_0 E^{-s}}{\pi^{3/2} R_{diff}^3} \exp\left(-\frac{R^2}{R_{diff}^2}\right) \text{ GeV}^{-1} \text{ cm}^{-3}, \quad (3)$$

where R is the distance from the center of the SNR and the injection spectrum is assumed to be a power-law, $Q \propto E^{-s} \delta(R) \delta(t)$. We also adopt Eq. (3) for electrons. The energy losses for protons and electrons are considered as described in Section 4.1.1. N_0 is the normalization and proportional to the total proton energy W_{tot} injected at $t = 0$ from the source. R_{diff} is the diffusion radius represented by $2\sqrt{D(E)(t - \chi(E))}$. $D(E)$ is the diffusion coefficient described by the following equation,

$$D(E) = D_{10} (E/10 \text{ GeV})^\delta \text{ cm}^2 \text{ s}^{-1}, \quad (4)$$

where D_{10} is the value of the diffusion coefficient at $E = 10 \text{ GeV}$. $\chi(E)$ represents the confinement of the particles until t_{Sedov} , where $\chi(E) = t_{Sedov} (E/E_{max})^{-1/\epsilon}$. ϵ determines the release time of the

particles with energy E . In the case of $t - \chi(E) \leq 0$, Eq. (3) becomes 0, i.e., particles are not released from the shell. We assume $t_{\text{sedov}} = 200$ yr and $E_{\text{max}} = 5$ PeV, where E_{max} is the highest energy of the accelerated particles in the SNR. These values vary depending on the environment of an SNR. However, this does not significantly affect our results.

For the formalism of Eq. (3), the injected particles below the threshold energy defined by $t - \chi(E) = 0$ remain completely within the SNR shell, while the rest are entirely released. This is not consistent with the particle spectrum obtained by the modeling of the GeV spectrum as described before; therefore, we extrapolate the particle spectrum above the threshold energy by using the broken power-law model. The index above the threshold is the same as the particle momentum spectrum used in Figure 4(a). This requires that the momentum break energy (~ 3 GeV c^{-1}) is consistent with the energy threshold of the escaped particles at the SNR age. Thus, ϵ is obtained to be 3.0. This approximation for the GeV spectrum reduces the amount of escaped particles just above the threshold compared to Eq. (3), but it does not greatly affect the modeling of the TeV emission since the energies of the contributing particles are much higher than the threshold.

We calculate the radiation model curves for the GeV emission with the same parameters as those of Figure 4(a). For the TeV emission, the radiation curves are calculated assuming $K_{ep} = 0.01$ and the typical values in a molecular cloud for the magnetic field of $10 \mu\text{G}$ and $\bar{n}_{\text{H}} = 100 \text{ cm}^{-3}$. The obtained radiation curves are shown in Figure 5. The amount of secondary e^+/e^- in the TeV-emitting clouds depends on \bar{n}_{H} of gas in which protons, i.e., parent particles of the secondaries, propagate, which is uncertain. If the gas is much denser than $\bar{n}_{\text{H}} = 100 \text{ cm}^{-3}$, then the emission from secondary e^+/e^- can contribute significantly to the radio spectrum. However, the resulting parameters from the modeling with the extremely dense gas are not largely affected with the exception of the magnetic field. Therefore, we neglect the contribution of emission from the secondaries in the TeV emission. To simplify the electron energy losses during the propagation,

we use the constant magnetic field and \bar{n}_H of the TeV-emitting clouds. This assumption affects only the peak energy of synchrotron emission, which is not constrained by any observations.

The value of δ is constrained to be 0.6 by fitting the particle spectrum to the TeV gamma-ray spectral slopes above the SED peak. D_{10} is constrained by the cutoff energy of the particle spectrum corresponding to the SED peak of the TeV emission since the cutoff energy is proportional to $R_{TeV}^2/R_{diff}^2 = R_{TeV}^2/[4D_{10}(E/10 \text{ GeV})^\delta (t - \chi(E))]$, where R_{TeV} is the distance to the TeV-emitting clouds. A lower limit on R_{TeV} can be provided by the radius of the radio shell of $\approx 26 \text{ (d/4 kpc) pc}$ since the TeV-emitting clouds should be located further from the remnant than the GeV-emitting clouds. As a result, the lower limit on D_{10} is obtained to be $7.5 \times 10^{25} \text{ (d/4 kpc)}^2 \text{ cm}^2 \text{ s}^{-1}$. The observed differential flux of the TeV emission is described by $F_{TeV} \propto W_{tot} D_{10}^{-3/2} 10^{3\delta/2} M_{TeV}/4\pi d^2$ using Eq. (3) and (4), where M_{TeV} is the mass of the clouds responsible for the observed TeV emission. Using the above relation, we can obtain an upper limit on D_{10} from the mass obtained by the CO(J = 1–0) data with NANTEN. We searched for the TeV-emitting clouds in the velocity range from 10 to 40 km s^{-1} , corresponding to the distance to G8.7–0.1 and found molecular clouds with the mass of about $2.0 \times 10^6 M_\odot$ for the velocity range from 10 to 30 km s^{-1} . Thus, an upper limit on D_{10} is $5.4 \times 10^{26} \cdot [(W_{tot}/10^{50} \text{ erg}) \cdot (4 \text{ kpc/d})^2]^{2/3} \cdot (10^{(\delta/0.6)}/10) \text{ cm}^2 \text{ s}^{-1}$. In this case, R_{TeV} comes to $\sim 70 \text{ pc}$. The constrained range for D_{10} is much smaller than that obtained by Delahaye et al. (2008), where δ and D_{10} were estimated to be 0.46–0.70 and $0.6\text{--}6.7 \times 10^{28} \text{ cm}^2 \text{ s}^{-1}$ by using the observed ratios of secondary to primary nuclei. However, our results probably represent an environment of dense interstellar gas since a lower $D_{10} \sim 10^{26} \text{ cm}^2 \text{ s}^{-1}$ is expected in that case (Ormes et al. 1988).

We also consider other possible scenarios: 1) both the GeV and TeV gamma rays originate from the interaction escaped particles accelerated in G8.7–0.1 with molecular clouds, 2) the GeV emission arises from the mechanism predicted by Uchiyama et al. (2010). To examine the possibility of scenario 1), we perform the modeling for the GeV and TeV emission using Eq. (3).

As a result, D_{10} is constrained to be $4.0 \times 10^{27} (\text{d}/4 \text{ kpc})^2 \text{ cm}^2 \text{ s}^{-1}$ by the cutoff energy of the particle spectrum corresponding to the SED peak of the GeV emission, while δ is constrained to be 0.6 by fitting the particle spectra to the gamma-ray spectral slopes above the SED peaks. The model of the TeV emission using the obtained diffusion coefficient gives $M_{\text{TeV}} = 4.4 \times 10^7 M_{\odot}$, which is much larger than the observed value. Therefore, this scenario is unlikely. In the case of scenario 2), Uchiyama et al. (2010) state that TeV emission would not be explained by this mechanism and may instead arise from the interaction of particles that escaped from SNR shocks at earlier epochs with the molecular clouds. Thus, D_{10} does not change.

5. CONCLUSIONS

We have investigated the GeV gamma rays in the vicinity of the SNR G8.7–0.1 and found that they are extended. Most of the emission (Source E) is positionally coincident with the SNR G8.7–0.1, while a lesser portion (Source W), located outside the western boundary of G8.7–0.1, has no evident counterpart in other wavelengths within the 95% confidence region obtained using a point source model. The GeV gamma rays coincide with spatially-connected molecular clouds, implying a physical connection between the two sources. The decay of π^0 s produced by particles accelerated in the SNR and hitting the molecular clouds naturally explains the GeV gamma-ray spectrum since a direct interaction between G8.7–0.1 and the molecular clouds is supported by the detection of an OH maser, although electron bremsstrahlung cannot be ruled out.

On the other hand, the GeV morphology is not well represented by the TeV emission from HESS J1804–216. The GeV gamma-ray spectrum has a break around 2 GeV and falls below the extrapolation of the TeV gamma-ray spectrum of HESS J1804–216. The TeV spectral index is most naturally explained by a theory assuming the energy-dependent diffusion of particles accelerated in the SNR, although the possibility that the TeV emission might come from a PWN cannot be ruled out. Under the assumption that the bulk of the TeV gamma rays comes from

the interaction between distant molecular clouds and cosmic rays released and diffused from G8.7–0.1, we can constrain the diffusion coefficient of the particles.

The *Fermi* LAT Collaboration acknowledges generous ongoing support from a number of agencies and institutes that have supported both the development and the operation of the LAT as well as scientific data analysis. These include the National Aeronautics and Space Administration and the Department of Energy in the United States, the Commissariat à l’Energie Atomique and the Centre National de la Recherche Scientifique / Institut National de Physique Nucléaire et de Physique des Particules in France, the Agenzia Spaziale Italiana and the Istituto Nazionale di Fisica Nucleare in Italy, the Ministry of Education, Culture, Sports, Science and Technology (MEXT), High Energy Accelerator Research Organization (KEK) and Japan Aerospace Exploration Agency (JAXA) in Japan, and the K. A. Wallenberg Foundation, the Swedish Research Council and the Swedish National Space Board in Sweden.

Additional support for science analysis during the operations phase is gratefully acknowledged from the Istituto Nazionale di Astrofisica in Italy and the Centre National d’Études Spatiales in France.

REFERENCES

- Abdo, A. A., et al. (The *Fermi* LAT Collaboration) 2009, ApJ, 706, L1
- Abdo, A. A., et al. (The *Fermi* LAT Collaboration) 2010a, ApJ, 708, 1254
- Abdo, A. A., et al. (The *Fermi* LAT Collaboration) 2010b, Science, 327, 1103
- Abdo, A. A., et al. (The *Fermi* LAT Collaboration) 2010c, ApJ, 712, 459
- Abdo, A. A., et al. (The *Fermi* LAT Collaboration) 2010d, ApJS, 188, 405
- Abdo, A. A., et al. (The *Fermi* LAT Collaboration) 2010e, ApJ, 713, 146
- Abdo, A. A., et al. (The *Fermi* LAT Collaboration) 2010f, ApJS, 187, 460
- Abdo, A. A., et al. (The *Fermi* LAT Collaboration) 2010g, ApJ, 714, 927
- Abdo, A. A., et al. (The *Fermi* LAT Collaboration) 2010h, ApJ, 718, 348
- Abdo, A. A., et al. (The *Fermi* LAT Collaboration) 2010i, ApJ, 722, 1303
- Aharonian, F. A., Drury, L. O., & Völk, H. J. 1994, A&A, 285, 645
- Aharonian, F. A.; Atoyan, A. M. 1996, A&A, 309, 917
- Aharonian, F., et al. (The H.E.S.S. Collaboration) 2006, ApJ, 636, 777
- Atwood, W. B., et al. (The *Fermi* LAT Collaboration) 2009, ApJ, 697, 1071
- Atoyan A. M., Aharonian A. F., & Fölk, H. J. 1995, Phys. Rev. D, 52, 3265
- Bamba, A., et al. 2007, PASJ, 59, S209
- Blitz, L., Fich, M., & Stark, A. A. 1982, ApJS, 49, 183
- Brand, J., & Blitz, L. 1993, A&A, 275, 67

- Briskin, W. F., Carrillo-Barragán, M., Kurtz, S., & Finley, J. P. 2006, *ApJ*, 652, 554
- Brogan C. L., Gelfand, J. D., Gaensler, B. M., Kassim, N. E., & Lazio, T. J. W. 2006, *ApJ*, 639, L25
- Castro, D., & Slane, P. 2010, *ApJ*, 717, 372
- Chevalier, R. A. 1999, *ApJ*, 511, 798
- Clifton, T. R., & Lyne, A. G. 1986, *Nature*, 320, 43
- Cordes, J M., & Lazio, T. J. W. 2002 astro-ph/0207156
- de Jager, O. C., & Djannati-Ataï, A. 2008, arXiv:0803.0116
- Delahaye, T., Lineros, R., Donato, F., Fornengo, N., & Salati, P. 2008, *Phys. Rev. D*, 77, 063527
- Finley, J. P., & Oegelman, H. 1994, *ApJ*, 434, L25
- Gabici, S., & Aharonian, F. A. 2007, *ApJ*, 665, L131
- Gabici, S., Aharonian, F. A., & Casanova, S. 2009, *MNRAS*, 396, 1629
- Grondin, M.-H., Funk, S., Lemoine-Goumard, M., et al. 2011, *ApJ*, 738, 42
- Hewitt, J. W., & Yusef-Zadeh, F. 2009, *ApJ*, 694, L16
- Higashi, Y., et al. 2008, *ApJ*, 683, 957
- Hobbs, G., et al. 2002, *MNRAS*, 333, L7
- Hobbs, G., Lyne, A. G., Kramer, M., Martin, C. E., & Jordan, C. 2004, *MNRAS*, 353, 1311
- Kargaltsev, O., Pavlov, G. G., & Garmire, G. P. 2007, *ApJ*, 670, 643
- Kamae, T., Karlsson, N., Mizuno, T., Abe, T., & Koi, T. 2006, *ApJ*, 647, 692

Kassim & Weiler 1990, ApJ, 360, 184

Manchester, R. N., Hobbs, G. B., Teoh, A., & Hobbs, M. 2005, AJ, 129, 1993

Mattox, J. R., et al. , 1996, ApJ, 461, 396

Mizuno, A., & Fukui, Y. 2004, Milky Way Surveys: The Structure and Evolution of our Galaxy,
317, 59

Mori, M. 2009, Astroparticle Physics, 31, 341

Odegard, N. 1986, AJ, 92, 1372

Ohira, Y., Murase, K., & Yamazaki, R. 2011, MNRAS, 410, 1577

Ojeda-May, P., Kurtz, S. E., Rodríguez, L. F., Arthur, S. J., & Velázquez, P. 2002, Rev. Mexicana
Astron. Astrofis., 38, 111

Ormes, J. F., Ozel, M. E., & Morris, D. J. 1988, ApJ, 334, 722

Pittori, C., et al. 2009, A&A, 506, 1563

Porter, T. A., Moskalenko, I. V., Strong, A. W., Orlando, E., & Bouchet, L. 2008, ApJ, 682, 400

Rando, R. et al., arXiv:0907.0626

Reynolds, S. P. 2008, ARA&A, 46, 89

Slane, P., Castro, D., Funk, S., Uchiyama, Y., Lemiére, A., Gelfand, J. D., & Lemoine-Goumard,
M. 2010, ApJ, 720, 266

Takeuchi, T., et al. 2010, PASJ, 62, 557

Theureau, G., et al. 2005, A&A, 430, 373

Uchiyama, Y., Blandford, R. D., Funk, S., Tajima, H., & Tanaka, T. 2010, ApJ, 723, L122

Weltevrede, P., et al. 2010, PASA, 27, 64

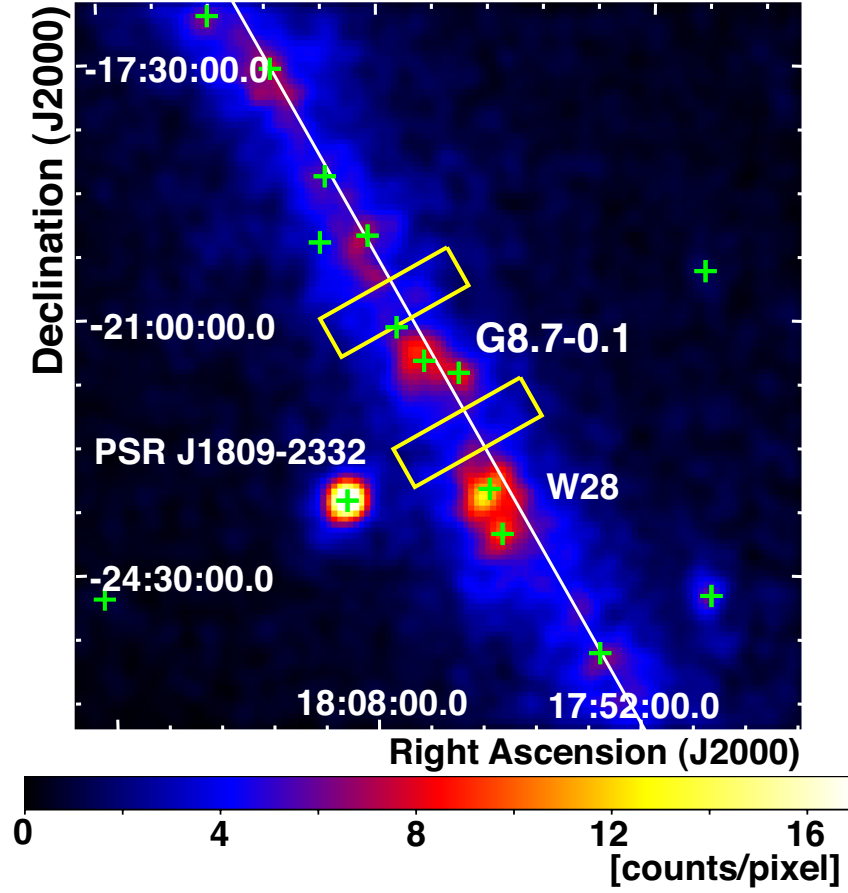


Fig. 1.— *Fermi* LAT 2-10 GeV counts map around the SNR G8.7-0.1. The count map is smoothed by a Gaussian kernel of $\sigma = 0^\circ 225$, with the pixel size of $0^\circ 075$. The green pluses indicate the sources in the 1FGL catalog (Abdo et al. 2010d). The yellow boxes indicate the regions that are used to evaluate the energy dependence for the systematic errors of the Galactic diffuse model. The white line from top left to bottom right indicates the Galactic plane.

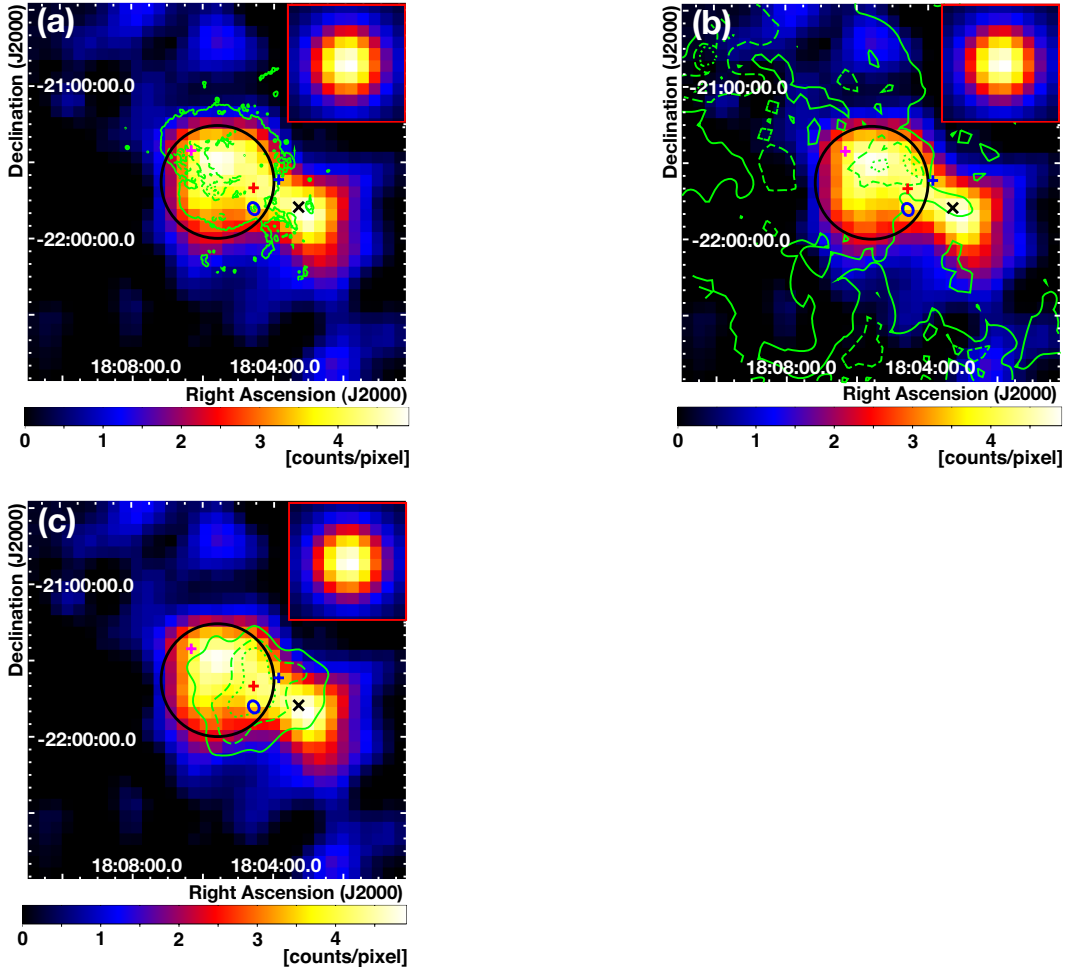


Fig. 2.— Close up views of the LAT 2–10 GeV counts map around G8.7-0.1 subtracting a fitted diffuse emission model including the isotropic component. The counts map has a pixel size of $0^{\circ}.075$ and is smoothed by a Gaussian kernel of $\sigma = 0^{\circ}.225$. The inset of each figure shows the effective LAT PSF for a photon spectral index of 2.5. A black circle in the east of each figure indicates the best-fit disk size for Source E. A black cross indicates the position of Source W. A blue and a magenta plus indicate PSR J1803–2137 and PSR J1806-2125, respectively. A red plus indicates the PWN candidate Suzaku J1804-2140. A blue ellipse indicates the radio extension of SNR G8.31–0.09 (Brogan 2006). Green contours in (a) show the VLA 90 cm image (Brogan 2006) at 5, 15, and 25% of the peak intensity. Green contours in (b) give CO ($J = 1-0$) line intensity taken by NANTEN (Mizuno & Fukui 2004; Takeuchi et al. 2010) at 25, 50, 75% levels, for the velocity range from 20 to 30 km s^{-1} , corresponding to kinematic distances of approximately 3.5 to 4.5 kpc. Green contours in (c) indicate the subtracted TeV photon counts of HESS J1804–216 at 25, 50 and 75% levels (Aharonian et al. 2006).

Table 1: Likelihood ratios for the different spatial models compared with the null hypothesis, no gamma-ray emission from G8.7–0.1 (2–10 GeV).

| Model | $-2 \ln(L_0/L)^a$ | Additional degrees of freedom |
|-----------------------------------|-------------------|-------------------------------|
| Null hypothesis | 0 | 0 |
| 3 point sources ^b | 433.4 | 12 |
| VLA 90 cm ^c + Source W | 436.5–462.4 | 6 |
| HESS ^c | 404.8–408.0 | 2 |
| Uniform disk and point source | 477.8 | 9 |
| PSR J1803–2137 ^d | 477.8 | 10 |

^a $-2 \ln(L_0/L)$, where L and L_0 are the maximum likelihoods for the model with/without the source component, respectively.

^bThree point sources listed in the 1FGL source catalog in the vicinity of the SNR G8.7–0.1, which their positions were free in the optimization.

^cThe values are obtained by using the spatial templates from the various extracted regions, where the regions were determined by changing a lower limit from 0 to 15% of the peak emission.

^dA point source model which is added to the Uniform disk and point source model.

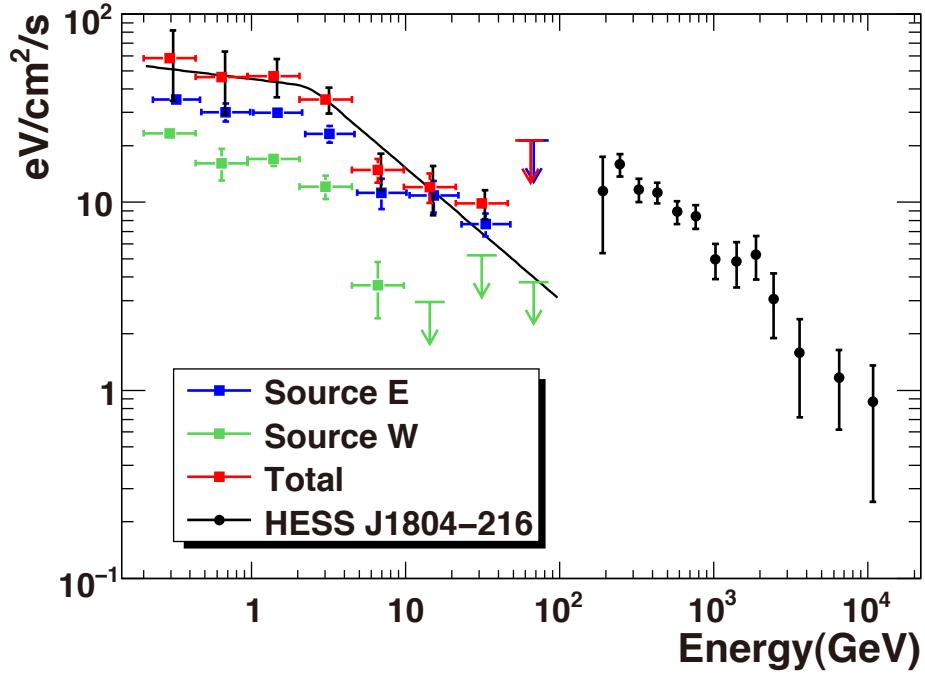


Fig. 3.— Spectral energy distribution of the *Fermi* LAT sources associated with G8.7–0.1. The blue and green squares with statistical error bars are the LAT fits for Source E and Source W, respectively. The red squares in the GeV regime are the total flux of the LAT data for both sources. Vertical bars in red and in black in the GeV band show the statistical errors and systematic errors of the total flux, respectively. Upper limits are obtained at the 90% confidence level in energy bins in which the likelihood test statistic is < 9 or the number of photons predicted by the best-fit model is less than 10. The black line shows the best-fit broken power-law model for the total spectrum. The black circles represent data points for HESS J1804–216 (Aharonian et al. 2006).

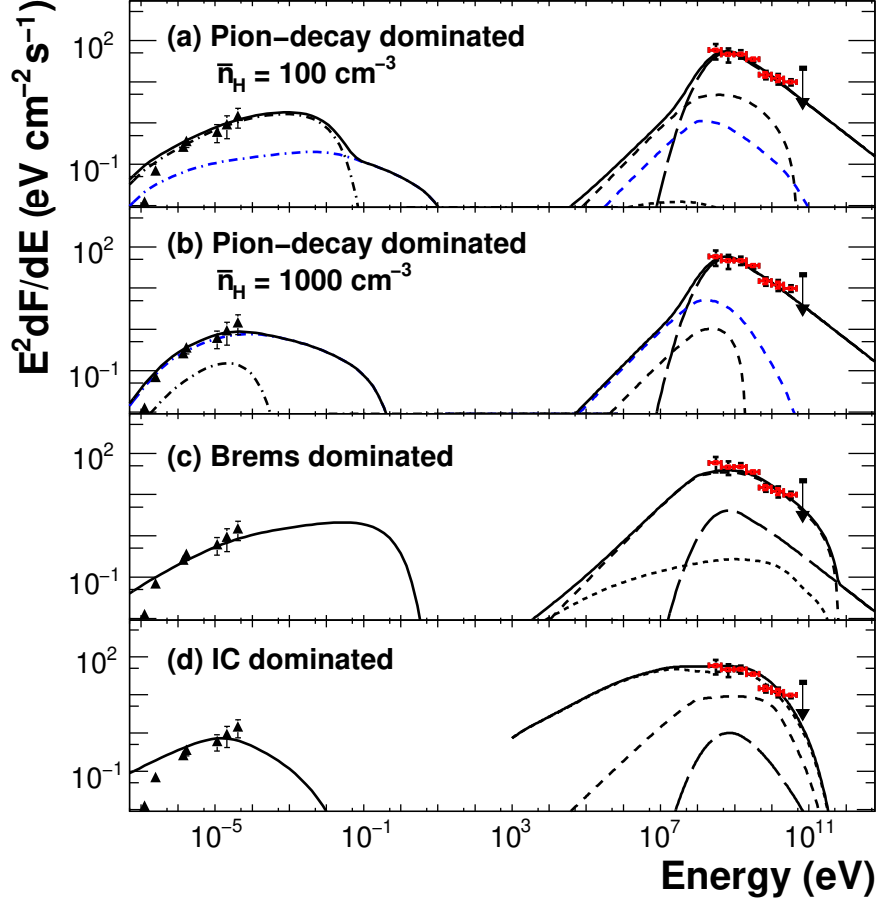


Fig. 4.— Multi-band spectra of the *Fermi* LAT emission associated with SNR G8.7–0.1. The red squares in GeV regime are the LAT data, where the red and black bars are the statistical and systematic errors, respectively. The radio emission from the entire region of G8.7–0.1 (Kassim & Weiler 1990) is modeled by synchrotron radiation, while the gamma-ray emission is modeled by different combinations of π^0 -decay (long-dashed curve), bremsstrahlung (dashed curve), and inverse Compton (IC) scattering (dotted curve). In the panel of (a), (b) and (c), the blue curves show the emission from the secondary e^+/e^- , and the dot-dashed lines in the radio band show the emission from the primary electrons and secondary e^+/e^- . Details of the models are described in the text.

Table 2: Parameters of the models for the *Fermi* LAT sources.

| Model | K_{ep} ^a | s_L ^b | p_b ^c | s_H ^d | B | \bar{n}_H ^e | W_p ^f | W_e ^f |
|---|-----------------------|--------------------|--------------------|--------------------|------------|--------------------------|------------------------|------------------------|
| | | | (GeV c^{-1}) | | (μ G) | (cm ⁻³) | (10 ⁴⁹ erg) | (10 ⁴⁹ erg) |
| (a) Pion ($\bar{n}_H = 100 \text{ cm}^{-3}$) | 0.01 | 2.0 | 3 | 2.7 | 100 | 100 | 2.8 | 4.6×10^{-2} |
| (b) Pion ($\bar{n}_H = 1000 \text{ cm}^{-3}$) | 0.01 | 2.0 | 3 | 2.7 | 400 | 1000 | 0.30 | 7.2×10^{-4} |
| (c) Bremsstrahlung | 1 | 2.0 | 5 | 2.7 | 25 | 100 | 0.22 | 0.36 |
| (d) Inverse Compton ^g | 1 | 2.0 | 15 | 3.5 | 1 | 0.1 | 48 | 99 |

^aThe ratio of electron and proton distribution functions at 1 GeV c^{-1} .

^bThe momentum distribution of particles is assumed to be a broken power-law, where the indices and the break momentum are identical for both accelerated protons and electrons. s_L is the spectral index below the momentum break.

^c p_b is the momentum break for the particle distribution.

^dThe spectral index for the broken power-law function above the momentum break.

^eAverage hydrogen number density of the ambient medium.

^fThe distance is assumed to be 4 kpc. The total energy is calculated for particles $> 100 \text{ MeV } c^{-1}$.

^gSeed photons for inverse Compton scattering of electrons include the cosmic microwave background, two infrared ($T_{\text{IR}} = 37, 4.7 \times 10^2 \text{ K}$, $U_{\text{IR}} = 1.1, 0.23 \text{ eV cm}^{-3}$, respectively), and two optical components ($T_{\text{opt}} = 3.3 \times 10^3, 9.5 \times 10^3 \text{ K}$, $U_{\text{opt}} = 1.2, 0.32 \text{ eV cm}^{-3}$, respectively) in the vicinity of G8.7–0.1, assuming a distance of 4 kpc.

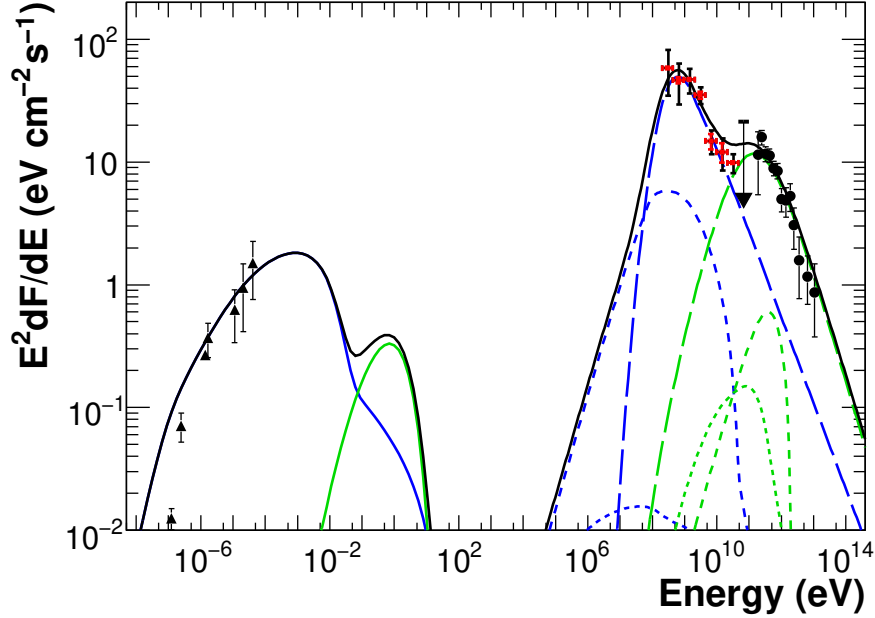


Fig. 5.— Comparison of the model results for the GeV and TeV gamma-rays with the observed spectra. The red squares in GeV regime are the LAT data, where the red and black bars are statistical and systematic errors, respectively. The black triangles show the radio emission from the entire region of G8.7–0.1 (Kassim & Weiler 1990). The TeV emission from HESS J1804–216 (Aharonian et al. 2006) is shown by the black circles. The solid black curve shows the total emission of the gamma-rays. The blue curves show the emission from the molecular clouds responsible for the GeV emission, which is a sum of emission from primary e^- and secondary e^-/e^+ . The green curves show the emission from the TeV-emitting clouds. The radio emission is modeled by synchrotron radiation (solid curves), while the gamma-ray emission is modeled by different combinations of π^0 -decay (long-dashed curve), bremsstrahlung (dashed curve), and inverse Compton (IC) scattering (dotted curve).